

A self-lensing binary massive black hole interpretation of quasi-periodic eruptions

Adam Ingram *, Sara E. Motta , Suzanne Aigrain and Aris Karastergiou

Department of Physics, Astrophysics, University of Oxford, Denys Wilkinson Building, Keble Road, Oxford OX1 3RH, UK

Accepted 2021 February 26. Received 2021 February 23; in original form 2020 November 16

ABSTRACT

Binary supermassive black hole (SMBH) systems result from galaxy mergers, and will eventually coalesce due to gravitational wave (GW) emission if the binary separation can be reduced to $\lesssim 0.1$ pc by other mechanisms. Here, we explore a gravitational self-lensing binary SMBH model for the sharp (duration ~ 1 h), quasi-regular X-ray flares – dubbed quasi-periodic eruptions – recently observed from two low-mass active galactic nuclei: GSN 069 and RX J1301.9+2747. In our model, the binary is observed \sim edge-on, such that each SMBH gravitationally lenses light from the accretion disc surrounding the other SMBH twice per orbital period. The model can reproduce the flare spacings if the current eccentricity of RX J1301.9+2747 is $\epsilon_0 \gtrsim 0.16$, implying a merger within ~ 1000 yr. However, we cannot reproduce the observed flare profiles with our current calculations. Model flares with the correct amplitude are $\sim 2/5$ the observed duration, and model flares with the correct duration are $\sim 2/5$ the observed amplitude. Our modelling yields three distinct behaviours of self-lensing binary systems that can be searched for in current and future X-ray and optical time-domain surveys: (i) periodic lensing flares, (ii) partial eclipses (caused by occultation of the background mini-disc by the foreground mini-disc), and (iii) partial eclipses with a very sharp in-eclipse lensing flare. Discovery of such features would constitute very strong evidence for the presence of a supermassive binary, and monitoring of the flare spacings will provide a measurement of periastron precession.

Key words: black hole physics – gravitational lensing: micro – gravitational waves – galaxies: Seyfert.

1 INTRODUCTION

Remarkably sharp, high-amplitude, regular flares – dubbed quasi-periodic eruptions (QPEs) – have recently been discovered in the X-ray light curves of two low-mass active galactic nuclei (AGNs): GSN 069 (Miniutti et al. 2019) and RX J1301.9+2747 (hereafter RX J1301; Giustini, Miniutti & Saxton 2020). Both AGNs have been optically classified as Seyfert 2 galaxies (Sun, Shu & Wang 2013; Shu et al. 2018), and both exhibit a thermal X-ray spectrum consistent with a standard thin accretion disc (Shakura & Sunyaev 1973) around a black hole (BH) of mass $M \sim 10^{5-6} M_{\odot}$. In GSN 069, QPEs are observed in *XMM-Newton* and *Chandra* data from 2018 and 2019 to have a duration of ~ 1 h and a spacing of ~ 9 h, and the peak 0.2–2 keV count rate is ~ 1 order of magnitude higher than the quiescent level. There is evidence that the true period in GSN 069 is ~ 18 h, with a larger flare being followed by a smaller flare just over 9 h later, followed by another flare just under 9 h later, and so on (Miniutti et al., in preparation).

Similar flares in the X-ray light curve of RX J1301 had previously been seen in an *XMM-Newton* observation from 2000, a *Chandra* observation from 2009, and possibly *ROSAT* observations (Dewan et al. 2000) in the early-mid 1990s (Earth occultations make confirmation challenging). However, since no single observation contained more than one full flare, it was not possible to determine

whether or not the flares were periodic until a recent *XMM-Newton* observation that revealed the same large-flare-followed-by-small-flare behaviour exhibited by GSN 069, except the long and short waiting times are in this case ~ 5.6 and ~ 3.6 h, respectively (Giustini et al. 2020). Since the full flare in the 2000 *XMM-Newton* observation is preceded at the start of the exposure by the tail end of the previous flare ~ 5 h earlier, it appears that the QPE spacings in RX J1301 have evolved over a 19 yr time-scale.

Such sharp flares are unlikely to be driven by changes in the accretion rate on to the BH, since even a δ -function perturbation in accretion rate will be smoothed on approximately the viscous time-scale by the effective viscosity of the disc (Lynden-Bell & Pringle 1974; Frank, King & Raine 2002; Mushtukov, Ingram & van der Klis 2018). The viscous time-scale for a disc around an $M \sim 10^5 M_{\odot}$ BH is hundreds of hours, which is far larger than the ~ 1 h duration of the QPE flares. Although variability on time-scales shorter than the viscous time-scale is possible, short accretion flares are expected to have a fast rise with an exponential decay, whereas the QPE flares are remarkably symmetric (Miniutti et al. 2019).

Here, we explore a model whereby GSN 069 and RX J1301 are both close binary massive BH systems. Such systems are thought to be surrounded by a circumbinary disc with inner edge $\approx 2r_a(1 + \epsilon)$ (e.g. Pringle 1991; MacFadyen & Milosavljević 2008; D’Orazio, Haiman & MacFadyen 2013), where r_a and ϵ are, respectively, the semimajor axis and eccentricity of the binary, and each BH is thought to be surrounded by its own mini-disc (e.g. Farris et al. 2014; Shi & Krolik 2015; Bowen et al. 2017, 2018; Ryan & MacFadyen 2017;

* E-mail: adam.ingram@physics.ox.ac.uk

d’Ascoli et al. 2018). If the system is viewed from a high inclination angle (i.e. nearly edge-on), one BH will pass in front of the other twice per orbit, leading the foreground BH to lens light from the background BH’s mini-disc (D’Orazio & Di Stefano 2018). There will therefore be two flares per orbit. The implied orbital periods ($P \sim 18$ h for GSN 069 and $P \sim 9$ h for RX J1301) are very short, requiring both systems considered here to be very close binaries (r_a as small as hundreds of gravitational radii). The larger flare will occur when the primary acts as the lens for two reasons: (1) the more massive BH is a stronger gravitational lens, and (2) the accretion rate on to the secondary is thought to be larger than that on to the primary (Farris et al. 2014; Duffell et al. 2020). The latter point also implies that the mass ratio, $q = M_2/M_1$, is likely to have been driven close to unity by enhanced accretion on to the secondary over the long period of time taken for gravitational wave (GW) emission to evolve these systems to such a small separations. This provides a natural explanation for why the amplitude of the large flare is only just greater than that of the small flare in both objects. The long and short waiting times between flares can be explained by an eccentric orbit (although a small eccentricity is expected after prolonged accretion; Zrake et al. 2021). Our model is similar to one recently applied to the AGN nicknamed ‘Spikey’ (Hu et al. 2020; Kun, Frey & Gabányi 2020), except in that case the inferred orbital period was far longer (~ 418 d). In this paper, we explore two tests of our binary interpretation of QPEs. In Section 2.2, we study the evolution of the QPE flares in RX J1301 over the 19 yr from 2000 to 2019, and in Section 3 we develop a quantitative model for the self-lensing flare profiles and compare the properties of the model to those of the GSN 069 QPE flares. We discuss our results in Section 4 and finally conclude in Section 5.

2 BINARY SYSTEM LIMITS ON RX J1301

In this section, we explore the limits we can put on the binary parameters if the binary BH hypothesis is to reproduce the observed QPEs. We first calculate the minimum eccentricity required to explain the ratio between long and short waiting times of consecutive flares (Section 2.1). We then place limits on the binary parameters by comparing the observed long-term evolution of the QPEs with the expected orbital evolution due to GW emission (Section 2.2). RX J1301 is by far the most useful object for both of these tests.

2.1 Eccentricity

For both GSN 069 and RX J1301, the waiting time from large flare to small flare is greater than the waiting time from small to large flare. This can be explained within the lensing model if the orbit is eccentric, since in this case the orbital angular velocity changes with orbital phase. According to the coordinate system defined in Fig. 1, the small flare (secondary is the lens) occurs when the orbital phase is equal to the viewer azimuth, $\phi_* = \phi_i$, and the large flare (primary is the lens) occurs when $\phi_* = \phi_i + \pi$. The orbital angular velocity takes its maximum value at pericentre ($\phi_* = 0$). Therefore, the lensing model requires that both QPE sources happen to have $\pi < \phi_i < 2\pi$, but that sources discovered in the future are equally likely to display the opposite behaviour of the longer waiting time being after the small flare (which would result from $0 < \phi_i < \pi$).

In the 2019 observations of RX J1301, the short waiting time is ~ 13 ks, which is ~ 40 per cent of the orbit. We can determine the minimum orbital eccentricity required to explain this by first integrating the Keplerian expression for orbital angular velocity to

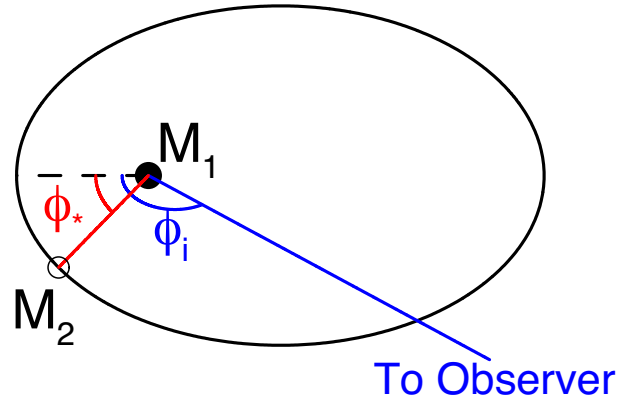


Figure 1. Binary system viewed from above the orbital plane in the rest frame of the primary, such that the secondary (open circle) orbits the primary (filled circle) with orbital phase ϕ_* , defined from pericentre (dashed line). The viewer azimuth ϕ_i is the angle between pericentre and the projection of the observer’s line of sight on the orbital plane (blue line).

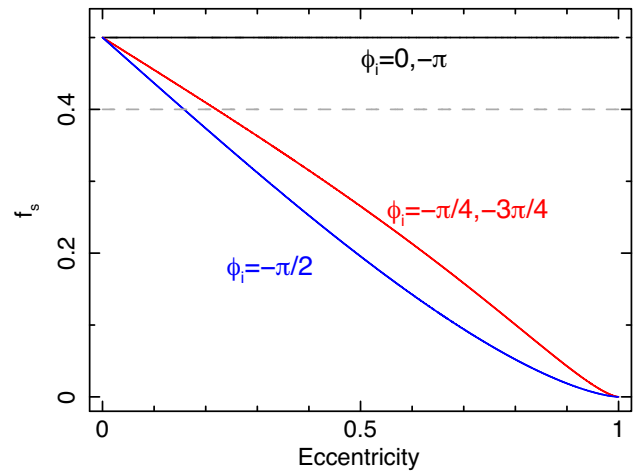


Figure 2. Fraction of the orbit occupied by the waiting time from the small flare (secondary is the lens) to the large flare (primary is the lens) as a function of orbital eccentricity, for different values of observer azimuth, ϕ_i (defined in Fig. 1). The grey dashed line depicts the value observed for RX J1301.

get the waiting time from pericentre to orbital phase ϕ_*

$$t(\phi_*) = \frac{P}{2\pi} \left\{ 2 \arctan \left[\sqrt{\frac{1-\epsilon}{1+\epsilon}} \tan \left(\frac{\phi_*}{2} \right) \right] - \frac{\epsilon \sqrt{1-\epsilon^2} \sin \phi_*}{1+\epsilon \cos \phi_*} \right\}. \quad (1)$$

The fraction of the orbit taken up by the short waiting time is then

$$f_s(\epsilon, \phi_i) = \frac{t(\phi_* = \phi_i + \pi) - t(\phi_* = \phi_i)}{P}. \quad (2)$$

Fig. 2 shows f_s plotted as a function of eccentricity for a range of ϕ_i values. The eccentricity for which this fraction takes the observed value $f_s = 0.4$ (grey dashed line) depends on ϕ_i . As can be seen in the plot, the minimum eccentricity for which $f_s = 0.4$ occurs is for $\phi_i = -\pi/2$, since in this case the interval between the small and large flare is exactly the portion of the orbit with the fastest orbital angular velocity. Therefore, the minimum eccentricity can be found by solving the equation $f_s(\epsilon_{\min}, \phi_i = -\pi/2) = 0.4$, yielding $\epsilon_{\min} \approx 0.16$. The eccentricity of RX J1301 in 2019, according to the lensing

model, is therefore $0.16 \lesssim \epsilon \lesssim 1$. No formal limits can be placed on the eccentricity of GSN 069 because the large and small flares are almost equally spaced. This is most likely caused by the orbit being nearly circular, but is formally compatible with any eccentricity as long as $\phi_i \sim 0$ or $\phi_i \sim \pi$.

2.2 Orbital evolution

We can also place limits on the binary parameters by comparing the observed long-term evolution of the QPEs with the expected orbital evolution due to GW emission. Again, RX J1301 is the most useful object for this test, because there is a ~ 19 yr baseline between the observation in 2000 and the recent observations.

The orbital separation and eccentricity will be reduced by energy lost through GW emission. The rate of change of the semilatus rectum, p , and the eccentricity are (Peters 1964; Gopakumar & Iyer 1997; Martel & Poisson 1999)

$$\frac{dp}{dt} = -\frac{64}{5} \frac{(1 - \epsilon^2)^{3/2}}{(p/r_g)^3} \left(1 + \frac{7}{8}\epsilon^2\right) \frac{M_1 M_2}{M^2} c, \quad (3)$$

and

$$\frac{d\epsilon}{dt} = -\frac{304}{15} \frac{(1 - \epsilon^2)^{3/2}}{(p/r_g)^4} \epsilon \left(1 + \frac{121}{304}\epsilon^2\right) \frac{M_1 M_2}{M^2} \frac{c}{r_g}, \quad (4)$$

respectively, where $r_g = GM/c^2$ is the gravitational radius of the binary system, $M = M_1 + M_2$, and c is the speed of light in a vacuum. We set an initial period and eccentricity, P_0 and ϵ_0 , and numerically evolve the above equations forwards or backwards in time from $t = 0$. The period and semilatus rectum are related by Kepler's law

$$P = \frac{2\pi}{(GM)^{1/2}} \left(\frac{p}{1 - \epsilon^2}\right)^{3/2}. \quad (5)$$

We verify our scheme by comparing our numerical solution of the time-dependent period for $\epsilon = 0$ with the analytic solution for period in the case of circular motion.

For the case of RX J1301, the short and long waiting times between flares in 2019 are, respectively, ~ 13 and ~ 20 ks. The 2000 observation only contains one full flare, but the tail end of the previous flare can be seen at the start of the observation ~ 18 ks before the full flare. If the waiting time between flares in the 2000 observation was the short waiting time, then the short waiting time has reduced from ~ 18 to ~ 13 ks in ~ 19 yr. We explore the allowed binary parameters by setting $P_0 = 33$ ks (the 2019 value) and trialling a range of present-day eccentricities $\epsilon_0 \geq 0.16$ and a range of binary system mass values, M (we set $q = 1$). For each combination of mass and eccentricity trialled, we evolve the binary system backwards 19 yr to obtain the period and eccentricity in 2000. The resulting waiting time between flares in 2000 is then also dependent on the viewer azimuth, ϕ_i . The 2019 value of ϕ_i is fixed by the observed f_s for a particular trail ϵ_0 value, but ϕ_i will have *changed* since 2000 due to periastron precession. The precession period is $\sim (2/3)\pi(r_a/r_g)(1 - \epsilon^2)P \sim 1$ yr (e.g. Key & Cornish 2011), and depends on a number of unknown quantities such as the spin parameters and spin alignment of the two BHs. The uncertainty in the periastron precession rate is therefore large enough for ϕ_i in 2000 to be completely unknown. Therefore, the values of P and ϵ obtained by evolving the binary system backwards give rise to a *range* of possible short waiting times, for ϕ_i in the range $0 < \phi_i < 2\pi$ (we do not see the peak of the first flare in 2000, therefore we do not know if it is larger or smaller than the full flare, therefore we do not know if $\phi_i < \pi$ or $\phi_i > \pi$). If the maximum possible short waiting time is less than 18 ks, or if

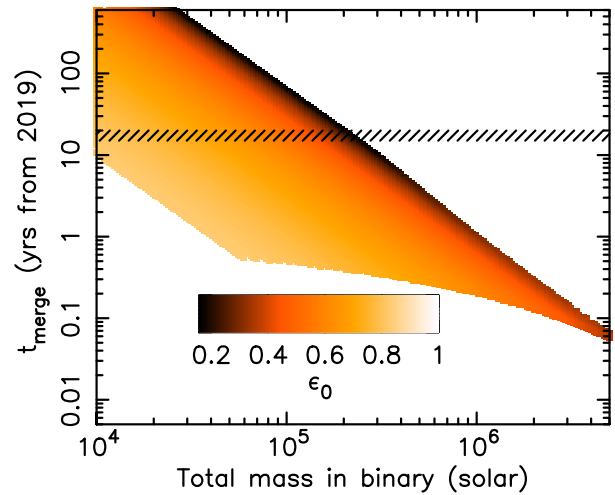


Figure 3. Future evolution of RX J1301 from 2019 in the binary hypothesis. Each combination of binary mass M and today's value of eccentricity ϵ_0 that is consistent with the evolution of spacing between QPE flares from 2000 to 2019 is plotted as a coloured square (colour represents ϵ_0 , see inset legend). The hatched markings depict the nominal mission lifetime of *LISA*.

the minimum possible waiting time is greater than 18 ks, then we discard the corresponding combination of ϵ_0 and M .

We then evolve all of the successful combinations of ϵ_0 and M forward from 2019 for 600 yr and determine if and when the BHs will merge. Fig. 3 displays the results. All points with a coloured square have a solution that can explain the evolution of RX J1301 from 2000 to 2019, and the colour of the square represents the eccentricity. Since eccentricity reduces with time, and the binary is old enough to have a small separation, we see the lower eccentricity solutions (dark squares) as the more plausible. We see that, as expected, lower mass binaries merge later. We only evolve the systems forward 600 yr, but extrapolating the trend from the figure gives $t_{\text{merge}} \sim 2500$ yr for $M = 10^4 M_\odot$. The hatched markings mark the nominal mission lifetime of the *Laser Interferometer Space Antenna (LISA)*; Amaro-Seoane et al. 2017) mission. We see that a fraction of our solutions merge during the lifetime of the *LISA* mission. *LISA* may also be sensitive to GWs from the binary before merger. In Fig. 4, we explore this possibility by taking the (most likely) $\epsilon_0 = 0.16$ solutions and evolving them forwards in time, calculating the characteristic GW strain as $h_c = 4\pi^{2/3}(GM_{\text{ch}})^{5/3}c^{-4}D^{-1}f^{2/3}$, where $f = 2/P$ is the GW frequency, D is the distance to the source (which we calculate from the redshift $z = 0.023$ assuming $H_0 = 74 \text{ km s}^{-1} \text{ Mpc}^{-1}$), and $M_{\text{ch}} = (M_1^3 M_2^3 / M)^{1/5}$ is the chirp mass (e.g. Misner, Thorne & Wheeler 1973). We then calculate the *LISA* signal-to-noise ratio (SNR) by dividing by the *LISA* noise (Robson, Cornish & Liu 2019, their equation 1) at the relevant GW frequency. We plot the peak value that this SNR reaches during the nominal 2034–2038 *LISA* lifetime as a function of binary mass (black line). We see that *LISA* will detect the binary for only a limited range of binary mass, for which the merger occurs during or shortly after the *LISA* mission. We repeat the same analysis for GSN 069 (red line), this time with $\epsilon_0 = 0$, $P_0 = 18$ h, and $z = 0.018$, and find that *LISA* will be able to detect the binary for a similarly narrow range of binary mass.

We do not yet have a long enough observational baseline to analyse the past evolution of the GSN 069 flares, but clearly future monitoring of the flare arrival times for both objects will enable us to better assess the feasibility of both being binary BH systems, and to determine the binary mass and therefore expected merger time. Useful constraints

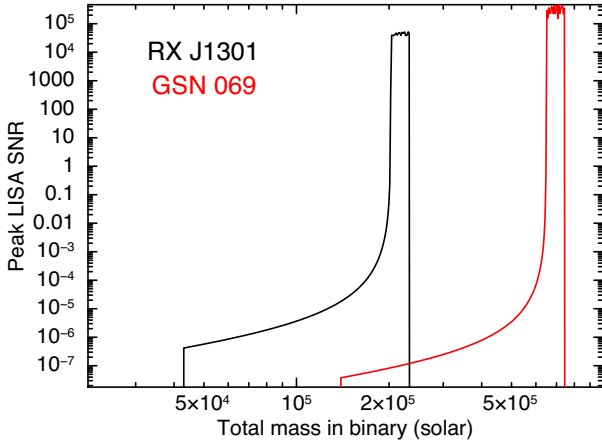


Figure 4. Peak SNR for measurements of GW strain from RX J1301 (black) and GSN 069 (red) that can be made by *LISA* during its operational lifetime (assumed to be 2034–2038) as a function of binary mass. We assume $\epsilon_0 = 0.16$ and $\epsilon_0 = 0$ for RX J1301 and GSN 069, respectively. The longer inferred orbital period of GSN 069 places it further away from merger for a given binary mass and therefore the binary must be more massive for it to merge during the *LISA* mission.

can be obtained with a baseline of a few years if flare arrival times relative to the flares in 2019 are measured as opposed to waiting times between consecutive flares. Our model predicts the relative spacings between small and large flares to change over a reasonably short time-scale due to periastron precession (period of ~ 1 yr for RX J1301). Dense monitoring of the flare arrival times would therefore yield a measurement of the periastron precession rate. Finally, if the flares stop, it could be either because the two BHs have merged, or because the binary has become close enough to tidal forces to disrupt the mini-discs (Haiman 2017; Tang, Haiman & MacFadyen 2018).

3 MODELLING THE GSN 069 QPES AS LENSING FLARES

We now calculate self-lensing flares for a high inclination binary supermassive BH (SMBH) system in order to compare with the QPE flares observed from GSN 069. We first briefly investigate the properties of the GSN 069 flares, and then describe the model, before exploring the flare profiles produced by the model, and we finally explore a large range of parameter space.

3.1 The GSN 069 flares

Here, our primary aim is to roughly determine basic properties of the GSN 069 flares that we aim to reproduce with our self-lensing model. We leave a comprehensive timing analysis to a later paper (Miniutti et al., in preparation). Fig. 5 shows a 0.4–2 keV light curve from GSN 069 folded on a period of 64.3555 ks and normalized to the quiescent level (black points). The large and small flares are clearly visible. We fit the flares with Gaussian functions and the quiescent flux with a constant frozen to unity (red lines). The best-fitting Gaussian parameters (quoted in the caption) indicate that the large and small flares have, respectively, a peak magnification of 7.055 and 5.49 and a full width at half-maximum (FWHM) of 1.35 and 1.62 ks.¹

¹Note that our model for each flare is a Gaussian function plus a unity quiescent level, so the peak magnification is $1 + N$ and the FWHM is $2\sigma\sqrt{2\ln[2N/(N-1)]}$

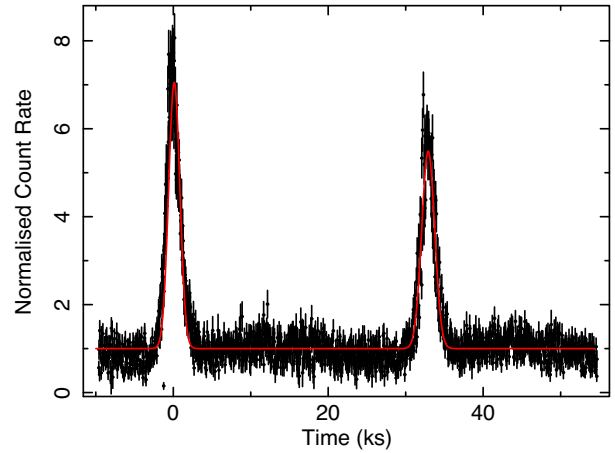


Figure 5. 0.4–2 keV *XMM-Newton* light curve of GSN 069 from 2019 January 16 folded on a period of 64.3555 ks and normalized to the quiescent level (black). The light curve includes three large flares and two small flares. We model the folded light curve with a constant (fixed to unity) plus two Gaussian components (red). The first Gaussian component represents the large flare (centroid = 0.1258 ks, width $\sigma = 0.722$ ks, normalization $N = 6.055$) and the second represents the small flare (centroid = 32.907 ks, $\sigma = 0.835$ ks, $N = 4.490$). The waiting time from large flare to small flare is therefore ~ 49 per cent of the period.

The waiting time from small flare to large flare is ~ 49 per cent of the period, compared with ~ 40 per cent for RX J1301. Our analysis here only considers the longest public *XMM-Newton* observation of the source (from 2019 January), which includes three large flares and two small flares. We see that the period appears to be stable over this observation. Overall, there are 15 flares in publicly available data, distributed over three *XMM-Newton* observations and one *Chandra* observation, covering a duration of ~ 5 months. The period is less stable over this longer time-scale, displaying small but noisy timing residuals compared to a model with a constant or smoothly evolving period (Miniutti et al., in preparation). The flare amplitude increases dramatically with energy band (see figs 2 and 3 of Miniutti et al. 2019).

3.2 Self-lensing model

Fig. 6 illustrates the geometry of our model. The source (background) BH, mass M_s , is pictured at the origin, with the lensing (foreground) BH, mass M_l , orbiting it. We define the mass ratio as $q = M_l/M_s$. The orbit is in general elliptical with semimajor axis r_a , although we go on to only explore circular orbits in the following subsection. The binary orbital axis is marked as $\hat{\mathbf{z}}_{\text{bin}}$, and pericentre is marked by the vector $\hat{\mathbf{x}}_{\text{bin}}$. The vector $\hat{\mathbf{o}}$ points from the source BH to the observer, such that the inclination angle i is the angle between $\hat{\mathbf{z}}_{\text{bin}}$ and $\hat{\mathbf{o}}$. The viewer azimuth, ϕ_i , is the angle between $\hat{\mathbf{x}}_{\text{bin}}$ and the projection of $\hat{\mathbf{o}}$ on to the binary plane. For circular orbits, we simply choose $\phi_i = 0$. The vector \mathbf{r}_* points from the source BH to the lens BH, such that its orientation moves anticlockwise around the binary plane as the orbital phase ϕ_* increases.

Each BH has an associated mini-disc. The vectors $\hat{\mathbf{z}}_s$ and $\hat{\mathbf{z}}_l$ denote the rotational axis for the background and foreground mini-discs, respectively. These vectors are defined by the angles δ_s , γ_s , δ_l , and γ_l , where $\cos \delta_s = \hat{\mathbf{z}}_{\text{bin}} \cdot \hat{\mathbf{z}}_s$, γ_s is the angle between the projections of $\hat{\mathbf{z}}_s$ and $\hat{\mathbf{o}}$ on the binary plane, and δ_l and γ_l are defined similarly. The δ angles are therefore polar angles, and the γ angles are azimuthal

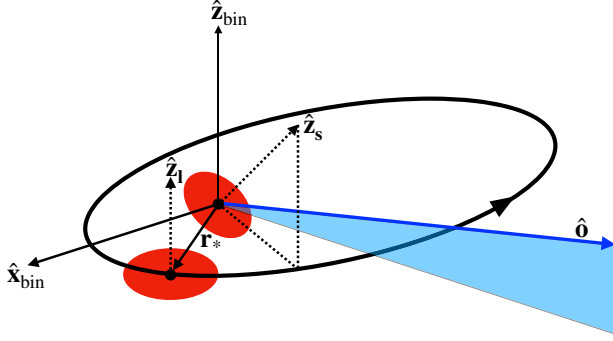


Figure 6. Schematic of our model geometry. A mini-disc (red) surrounds each BH (black circles). The primary is at the origin and the secondary follows an anticlockwise elliptical orbit in the plane perpendicular to $\hat{\mathbf{z}}_{\text{bin}}$, with a focus at the origin and pericentre when the vector connecting the two BHs, \mathbf{r}_* , aligns with $\hat{\mathbf{x}}_{\text{bin}}$. The observer’s line of sight is represented by the vector $\hat{\mathbf{o}}$ (blue). The rotation axis of the background and foreground mini-discs are, respectively, $\hat{\mathbf{z}}_s$ and $\hat{\mathbf{z}}_1$. In the case pictured, the background disc is tilted somewhat towards and to the left of the observer’s line of sight and the foreground disc aligns with the binary rotation axis.

angles (in a right-handed coordinate system). The mathematical details of our coordinate system are given in Appendix (A1).

We make the following assumptions about the geometry of the system:

- (i) The mini-discs are both stable over many binary orbits. This may not be the case for a particularly compact ($r_a \lesssim 60 r_g$) binary (Tang et al. 2018; Paschalidis et al. 2021).
- (ii) Each mini-disc is aligned with the corresponding BH spin axis. This may not be true in general, and a misalignment does influence the dynamics (Bardeen & Petterson 1975; Liska et al. 2019) and the observed spectrum (Abarr & Krawczynski 2020) of the disc, but we make this simplifying assumption in order to keep the problem tractable.
- (iii) The two BHs have the same dimensionless spin parameter, a , as one another. Again this is a simplifying assumption to keep the number of model parameters down.
- (iv) The inner radius of each mini-disc is at the innermost stable circular orbit (ISCO), which decreases with increasing spin parameter a (Bardeen, Press & Teukolsky 1972). This is thought to be the case for BH X-ray binaries in the soft state (e.g. Done, Gierlinski & Kubota 2007), for which the thermal spectrum is very similar to that of the QPE sources.
- (v) The outer edge of each mini-disc is $r_{\text{out}} = 0.25 r_a$. This is set by the dynamics of the binary system, including tidal forces and resonances (e.g. Artymowicz & Lubow 1994; Farris et al. 2014). We adopt the value approximately found by Bowen et al. (2017) in their relativistic simulations of a $q \sim 1$ binary system (see their table 3).
- (vi) The mini-discs are both circular and have well-defined outer edges. Bowen et al. (2017) note that this is not strictly the case in their simulations, with the outer edge on the near side of the other BH differing from that on the far side. We also ignore the streams of material flowing from the circumbinary disc to the mini-discs, and between the two mini-discs.
- (vii) The discs each radiate a multitemperature blackbody spectrum with a temperature profile $T(r) \propto r^{-3/4}[1 - \sqrt{r/r_{\text{in}}}]$, which corresponds to gravitational energy release with zero torque at the inner boundary (Novikov & Thorne 1973; Shakura & Sunyaev 1973). The peak disc temperature is a model parameter. We fix it to $kT_{\text{max}} = 50$ eV to match the spectrum of GSN 069 (Miniutti et al. 2019).

We first ray trace each disc individually in the Kerr metric. For each mini-disc, we define an image plane perpendicular to the observer’s line of sight, $\hat{\mathbf{o}}$, with the vertical axis $\hat{\beta}$ parallel to the projection of the disc spin axis on the image plane. The horizontal axis $\hat{\alpha}$ is perpendicular to both $\hat{\mathbf{o}}$ and $\hat{\beta}$, forming a right-handed coordinate system. The horizontal and vertical parameters on the image plane, α and β , are the impact parameters at infinity, and the BH is at the origin ($\alpha = \beta = 0$). Each point on the image plane, represented by the vector $\mathbf{b} = \alpha\hat{\alpha} + \beta\hat{\beta}$, corresponds to a unique null-geodesic in the Kerr metric. We trace rays backwards from a grid of (α, β) coordinates towards each BH, solving for the radius r that the geodesic crosses the equatorial plane of the BH. We use the publicly available code YNOGK, (Wang et al. 2012) which is based on the code GEOKERR (Dexter & Agol 2009).²

We then account for lensing of the background mini-disc by the foreground BH. This leads to each patch of the background mini-disc having two images: one inside (the internal image) and one outside (the external image) of the Einstein radius of the foreground BH, r_E . The position of the internal and external images on the observer plane are given, respectively, by the vectors \mathbf{b}_- and \mathbf{b}_+ . For simplicity, we ignore strong field effects, which is not necessarily a good assumption, but provides a good starting point to determine whether or not the model qualitatively works. In this case,

$$\mathbf{b}_{\pm} = \mathbf{b}_* + \frac{1}{2} \left[1 \pm \sqrt{1 + \left(\frac{2}{u}\right)^2} \right] (\mathbf{b} - \mathbf{b}_*), \quad (6)$$

where $u = |\mathbf{b} - \mathbf{b}_*|/r_E$ and \mathbf{b}_* is the projection of \mathbf{r}_* on the image plane (Paczynski 1996; Agol 2002; D’Orazio & Di Stefano 2018). The apparent area of each image is multiplied by a magnification factor

$$\mathcal{M}_{\pm} = \frac{1}{2} \left[\frac{u^2 + 2}{u\sqrt{u^2 + 4}} \pm 1 \right]. \quad (7)$$

The Einstein radius is given by $r_E = \sqrt{4r_{g\ell}\mathbf{r}_* \cdot \hat{\mathbf{o}}}$, where $r_{g\ell} = GM_{\ell}/c^2$. We account for Shapiro delays – caused by geodesics that are more heavily distorted by gravitational lensing having an increased path-length – with a simplified prescription described in Appendix (A2).

We calculate the time-dependent observed spectrum of the background mini-disc for a grid of time bins, and the spectrum of the foreground mini-disc (details in Appendix A3). We account for interstellar absorption using the XSPEC model TBABS (Wilms, Allen & McCray 2000). We fix the hydrogen column density to $N_{\text{H}} = 5 \times 10^{20} \text{ cm}^{-2}$, to match GSN 069 (Miniutti et al. 2019). We then fold the spectrum of the background mini-disc for each time bin, and also the constant spectrum of the foreground mini-disc, around the *XMM-Newton* EPIC-pn response matrix, and integrate the resulting counts spectra over the specified range of energy channels to create a light curve. We then add on the constant count rate of the foreground mini-disc and finally normalize to the quiescent level. Note that it is necessary to account for interstellar absorption because the response of *XMM-Newton* is not diagonal, especially in soft X-rays. Absorption can therefore lead to the soft X-ray energy channels being dominated by ‘misclassified’ higher energy photons. If the flare profile depends on energy, absorption will therefore influence the count rate as a function of time in a given energy channel, even on time-scales on which N_{H} is constant (Ingram et al. 2019).

²The ray-tracing code we used is also publicly available as part of the RELTRANS X-ray reverberation mapping code (Ingram et al. 2019).

We do not include Doppler modulation due to centre-of-mass motion of each mini-disc around the binary centre of mass. This does not contribute to the flare profile since the orbital motion of each BH is entirely transverse during the flares. The orbital motion should, however, contribute a periodic Doppler modulation outside of the flares (e.g. D’Orazio & Di Stefano 2018; Hu et al. 2020). For a \sim unity mass ratio, this modulation will be fairly subtle, since one BH is approaching the observer when the other is receding from the observer and so the summed flux from the two mini-discs will not be modulated as strongly as for $M_1 \gg M_2$. However, even for $q = 1$ there should still be a subtle Doppler modulation that peaks between flares since the approaching mini-disc should be boosted more strongly than the receding mini-disc is suppressed (specific flux is \propto Doppler factor to the third power).

3.3 Predicted flare profiles

We now explore the predicted flare profiles of our model. We consider the parameters relevant to GSN 069, specifically an orbital period of 18 h and a possible binary mass range of $\sim 5 \times 10^4 - 5 \times 10^6 M_\odot$.³ In order to reproduce the small difference between small and large QPE flares, we consider only binary parameters that would result in the two lensing flares per orbital period having the same profile. We therefore fix the mass ratio to $q = M_\ell/M_s = 1$, the eccentricity to $e = 0$, and set the misalignment angles of the two BHs equal to one another: $\delta_\ell = \delta_s = \delta$, $\gamma_\ell = \gamma_s = \gamma$. Although the large-flare-small-flare behaviour requires that q cannot be exactly unity, we note that the large flares are only ~ 30 per cent larger than the small flares (see Fig. 5) and so q must be *close* to unity. We only consider $q = 1$ in this section, since we are looking to explain the general properties of the flares. Any departures from $q = 1$ that make a significant difference to the flare profiles will also predict the large flare to be significantly larger than the small flare, which is not observed. We also note that the observed small noisy departures from a smoothly evolving period in the light curve can be explained as stochastic variations of the mini-disc structure, caused both by tidal forces and potentially relativistic precession.

Fig. 7 shows the predicted light curve for an aligned system ($\delta = 0$) of two Schwarzschild BHs with a total binary mass of $M = 10^6 M_\odot$, viewed from an inclination angle of $i = 89.5^\circ$. Red, green, and blue lines represent, respectively, the 0.2–0.3, 0.4–0.5, and 0.8–1.0 keV light curves, normalized to the quiescent-level count rate. Occultation by the foreground mini-disc is taken into account for the solid lines and ignored for the dashed lines. We see that the flare amplitude is comparable to that observed for QPEs (Fig. 5), but the duration is shorter. The QPE flares from GSN 069 (and indeed RX J1301) have a very strong energy dependence, with larger flares in higher energy bands (Miniutti et al. 2019). Our model does predict stronger flares in higher energy bands because the Doppler blue/red shifted (approaching/receding) side of the disc is magnified during the rising/falling phase of the flare. However, the resulting energy dependence shown in Fig. 7 is far more subtle than what is observed for QPEs.

³Note that the Miniutti et al. (2019) spectroscopic mass estimate of $M \sim 4 \times 10^5 M_\odot$ assumed a single disc inclined by 45° that extends to the ISCO of a Schwarzschild BH. Assuming the presence of a second disc, a higher inclination angle or a higher BH spin would *increase* the inferred mass, and so we see the range $M \gtrsim 4 \times 10^5 M_\odot$ as the most realistic, but the uncertainty is large enough to make it worth exploring significantly lower binary masses.

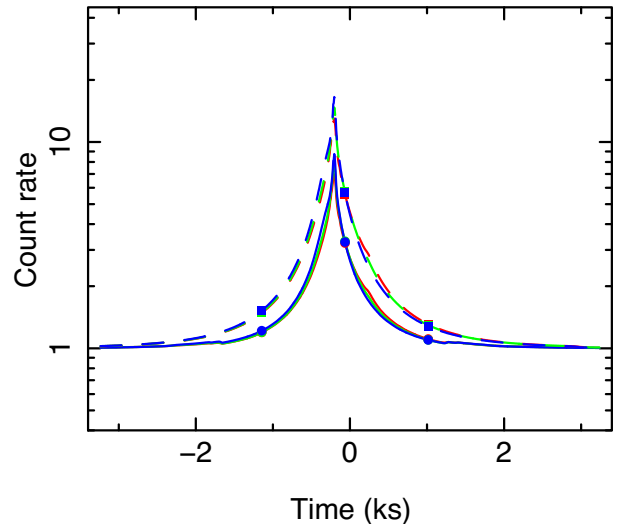


Figure 7. Light curves calculated for model parameters: $a = 0$, $\delta = 0^\circ$, $i = 89.5^\circ$, $M = 10^6 M_\odot$. Red, green, and blue lines represent the 0.2–0.3, 0.4–0.5, and 0.8–1.0 keV *XMM-Newton* count rate normalized to the quiescent level. The dashed lines ignore occultation by the foreground mini-disc and the solid lines account for it. The filled circles and squares denote the times for which images are plotted in Fig. 8.

Fig. 8 shows images of the system at three snapshots of time denoted by the solid circles in Fig. 7. The lensing (foreground) BH is at the origin, and its Einstein radius is represented by the dashed black line. The background mini-disc is coloured red and the outline of the foreground mini-disc, which eclipses any part of the background mini-disc that it passes in front of, is shown in grey. Note that the $\sim r^{-3}$ radial emissivity of the background mini-disc is not shown in these images, but *is* accounted for in our model. Distances are represented in units of $r_{g\ell} = GM_\ell/c^2$, and all images are oriented such that the rotation axis of the foreground mini-disc is vertical. We see that, from the top to the bottom panel, the background mini-disc moves from right to left, and is more heavily warped closer to the image plane than it is to the foreground BH. Each patch of the background mini-disc has an internal and an external image, one inside and one outside of the Einstein radius of the foreground BH. As a patch of the background mini-disc passes closer to the foreground BH, both images move closer to the Einstein radius and the magnification increases.

Occultation by the foreground mini-disc has little effect for the aligned case explored in Figs 7 and 8 because the projected image of the foreground mini-disc is largely *inside* of the Einstein radius. The foreground disc therefore cuts out almost none of the external image of the background disc, and only the lowest magnification part of the internal image. This is not the case for all parameter combinations. Fig. 9 shows the light curve for $a = 0$, $i = 89.5^\circ$, $\delta = 30^\circ$, $\gamma = 0^\circ$, and $M = 10^5 M_\odot$. The solid line now displays an eclipse down to half of the quiescent level (since half of the total flux is from the foreground disc) with no lensing flare at all. As Fig. 10 demonstrates, this is because the projection of the foreground mini-disc is now larger than the Einstein radius of the foreground BH, and so all of the magnified geodesics are cut out. The larger projected size of the foreground disc, relative to the Einstein radius of the foreground BH, is due partly to its lower inclination to the observer’s line of sight (i.e. $\beta = 30^\circ$, $\gamma = 0$ means that the mini-discs are viewed less edge-on than before). The lower binary mass is also important though because the disc outer radius, r_{out} , is proportional to the binary separation,

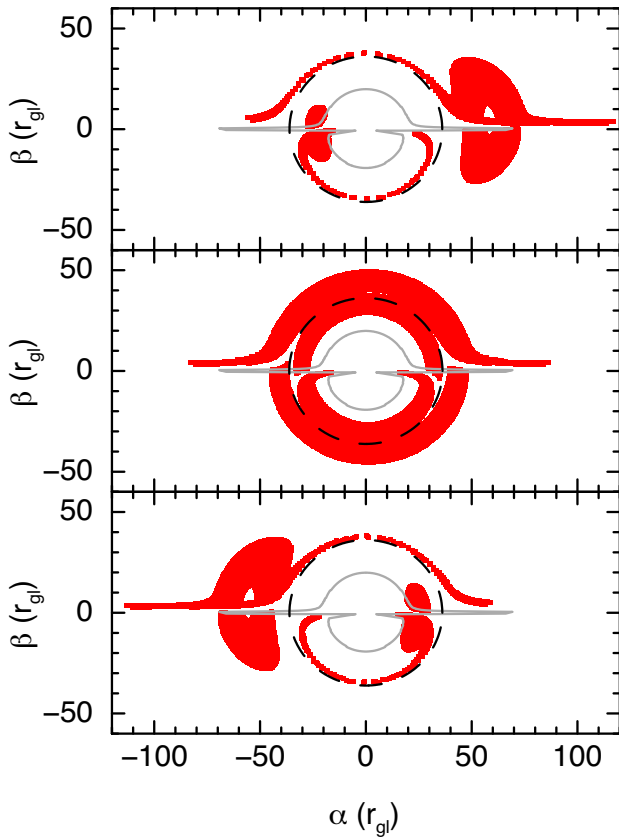


Figure 8. Images at three points in time denoted by the filled circles in Fig. 7. Model parameters are $a = 0$, $\delta = 0^\circ$, $i = 89.5^\circ$, and $M = 10^6 M_\odot$. The background mini-disc is shown in grey, the outline of the foreground mini-disc is in red, and the black dashed line denotes the Einstein radius of the foreground BH, which is always at the origin. The image is orientated such that the rotation axis of the foreground mini-disc is always vertical, and distances are expressed in units of $r_{\text{gl}} = GM_\ell/c^2$. The background mini-disc is warped by lensing around both the background and foreground BHs.

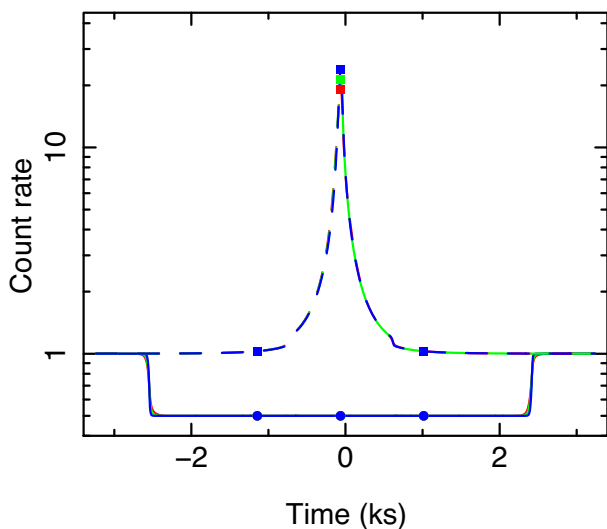


Figure 9. Light curves calculated for model parameters: $a = 0$, $\delta = 30^\circ$, $\gamma = 0^\circ$, $i = 89.9^\circ$, $M = 10^5 M_\odot$. We use the same plotting conventions as Fig. 7. For these parameters, occultation by the foreground mini-disc leads to an eclipse (solid lines). The filled circles denote the times for which images are plotted in Fig. 10.

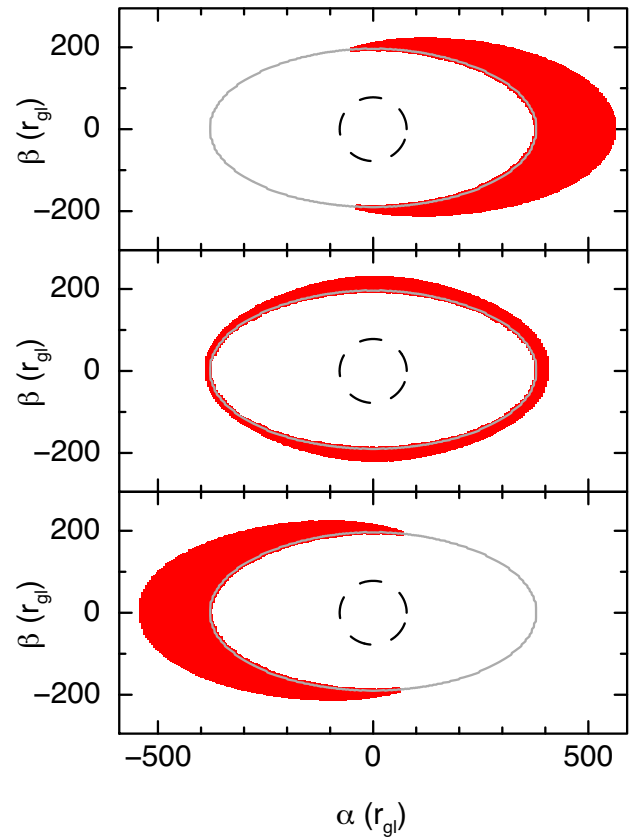


Figure 10. Images at three points in time denoted by the filled circles in Fig. 9. Model parameters are: $a = 0$, $\delta = 30^\circ$, $\gamma = 0^\circ$, $i = 89.9^\circ$, $M = 10^5 M_\odot$. We use the same plotting conventions as in Fig. 8.

r_a , whereas the Einstein radius is $r_E \propto r_{\text{gl}}^{1/2} r_a^{1/2}$. For a given orbital period and mass ratio, Kepler's law therefore gives $r_E/r_{\text{out}} \propto M^{1/3}$, and so occultation will matter less for higher mass systems.

There are also parameter combinations for which an eclipse with a sharp central lensing flare is predicted. Figs 11 and 12 show the light curve and images for such an example ($a = 0$, $i = 89.9^\circ$, $\delta = 10^\circ$, $\gamma = 50^\circ$, and $M = 10^5 M_\odot$). In this case, we see from Fig. 12 that the foreground disc cuts out all but a small fraction of the internal image, but the part of the image that is not cut out is closest to the Einstein radius and is therefore highly magnified. The flare is therefore very sharp indeed, with a large amplitude.

3.4 Parameter space exploration

We now explore parameter space to determine whether our model can reproduce the light curve of GSN 069. We aim to investigate whether the model can reproduce the basic flare properties averaged over large and small flares when we set $q = 1$; in the knowledge that any departure from unity mass ratio will naturally reproduce the observed large-flare-small-flare behaviour. From our fit to the folded light curve in Fig. 5, the average peak magnification is ≈ 6.3 and the average FWHM is ≈ 1.5 ks. We are interested both in whether the model can reproduce these properties at all and also how commonly it reproduces these values, which tells us the level of fine-tuning required for the model to explain the observed QPEs. Our model has five free parameters: a , M , i , δ , and γ . This represents a large

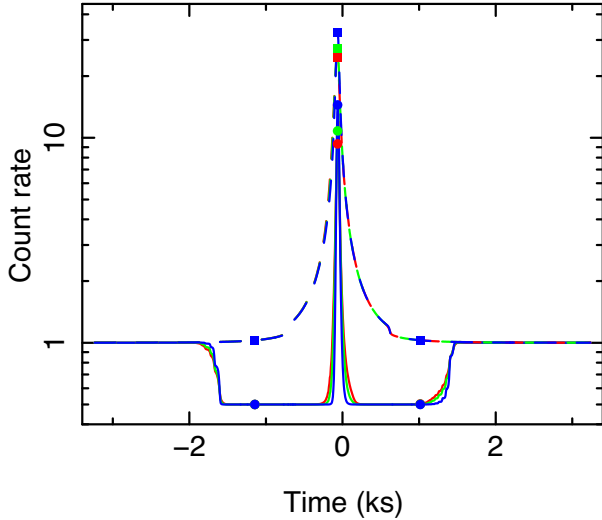


Figure 11. Light curves calculated for model parameters: $a = 0$, $\delta = 10^\circ$, $\gamma = 50^\circ$, $i = 89.9^\circ$, $M = 10^5 M_\odot$. We use the same plotting conventions as Fig. 7. For these parameters, the light curve features an eclipse and a sharp lensing flare (solid lines). The filled circles denote the times for which images are plotted in Fig. 12.

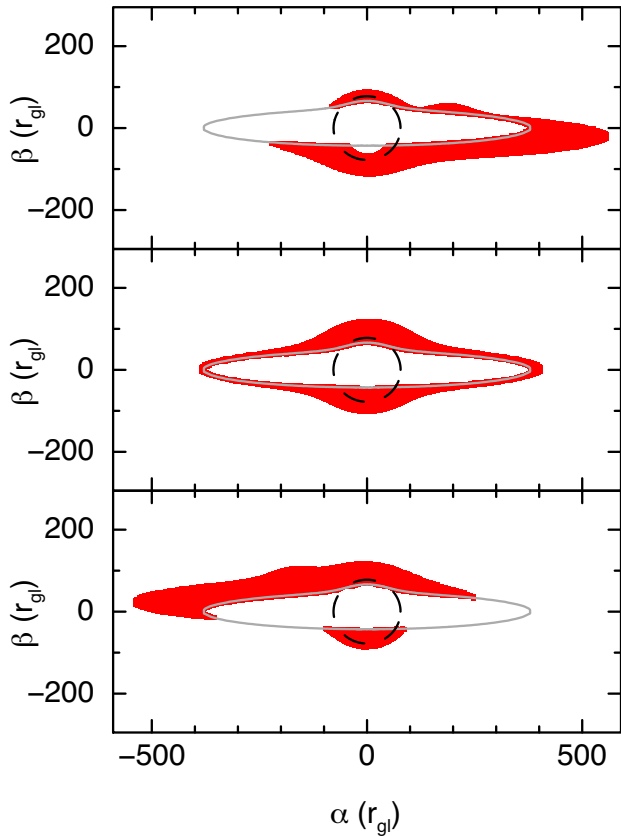


Figure 12. Images at three points in time denoted by the filled circles in Fig. 11. Model parameters are: $a = 0$, $\delta = 10^\circ$, $\gamma = 50^\circ$, $i = 89.9^\circ$, $M = 10^5 M_\odot$. We use the same plotting conventions as in Fig. 8. We see that the background mini-disc is lensed both around the background BH (the hump at $\alpha \sim 200 r_g$ in the top panel and $\sim -200 r_g$ in the bottom panel) and the foreground BH.

parameter space to explore with a single grid, and so we explore a grid of i and M values for a few fixed combinations of a , δ , and γ .

Fig. 13 is for an aligned binary system ($\delta = \gamma = 0^\circ$) with BH spin parameter $a = 0$ (left) and $a = 0.998$ (right). We trial a mass range of $M = 5 \times 10^4 - 5 \times 10^6 M_\odot$, with larger markers representing larger mass values, and an inclination range of $i = 87.5^\circ - 90^\circ$ (colour coded). The black cross represents the QPEs observed from GSN 069. We see that the aligned model cannot produce lensing flares simultaneously as long and as bright as the GSN 069 QPEs. For a given binary mass, the flare peak and FWHM are anticorrelated with one another, and increasing the inclination increases the peak while decreasing the FWHM. Increasing the mass moves the trend line closer to the top-right of the diagram (i.e. closer to the peak and FWHM values of GSN 069) for the lower inclination angles, whereas the mass dependence becomes more complex as the inclination angle approaches 90° . The flares tend to be more powerful for the case of high spin, since the ISCO is smaller and therefore the background source is more compact and so can be more efficiently lensed.

We additionally trial a number of parameter combinations with non-zero values of the misalignment angle, δ , all assuming maximal spin. In order to maximize the flare amplitude, we trial parameter combinations in which the very inner (i.e. brightest) regions of the background mini-disc can be lensed without being occulted by the foreground mini-disc. In Fig. 14, we explore configurations whereby we view the underside of the foreground and background mini-discs (i.e. $\gamma = 180$). The left-hand and right-hand panels are for $\delta = 0.5^\circ$ and $\delta = 1^\circ$, respectively. We see the same problem, in that the model cannot produce flares that are both large and long, only one or the other. In Fig. 15, we explore two configurations whereby we view both mini-discs exactly edge-on ($\gamma = 90^\circ$). The left-hand and right-hand panels are for $\delta = 70^\circ$ and $\delta = 90^\circ$, respectively (plus we also tried $\delta = 30^\circ$ with similar results).

Of all the parameter combinations trialled, we have been unable to find one which produces a flare with amplitude $\mathcal{M} \geq 6$ and FWHM ≥ 1.5 ks. In order to determine which parameter combination gets the closest to these values, we evaluate the statistic $\Delta = \sqrt{(\mathcal{M}/6.3 - 1)^2 + (\text{FWHM}/1.5 \text{ ks} - 1)^2}$ and take the combination with the minimum Δ to be the best. For the aligned model ($\delta = 0$), Δ is minimized for $a = 0.998$, $M = 5 \times 10^6 M_\odot$, and $i = 87.63^\circ$ ($\Delta = 0.6$). The overall minimum Δ is achieved for $\delta = 90^\circ$, $\gamma = 90^\circ$, $a = 0.998$, $M = 5 \times 10^6 M_\odot$, and $i = 87.5^\circ$ ($\Delta = 0.59$). We plot the 0.4–2 keV flare profile for both of these models in Fig. 16. The black lines represent the aligned model, and the red lines the $\delta = 90^\circ$ model. The dashed lines are without occultation and solid lines are with it. We see that, at least in the aligned case, the model gets a lot closer to reproducing the GSN 069 QPE flares (represented by the grey dashed line) if occultation is ignored than when it is accounted for. It may therefore be possible for the model to work if the mini-disc were optically thin (i.e. more like an X-ray corona), which would give flare profiles somewhere between the dashed and solid lines. However, the observed spectrum is well described by a multitemperature blackbody – which requires the discs to be optically thick. Moreover, the energy dependence is still too subtle to explain the observations. We also note that the high mass employed for this plot implies that the binary in GSN 069 would have already merged by now ($t_{\text{merge}} \approx 1.2$ yr).

4 DISCUSSION

We have explored a self-lensing binary BH model for the QPEs observed from two low-mass AGN: GSN 069 and RX J1301. We find that the ~ 19 yr evolution of the waiting time between consecutive

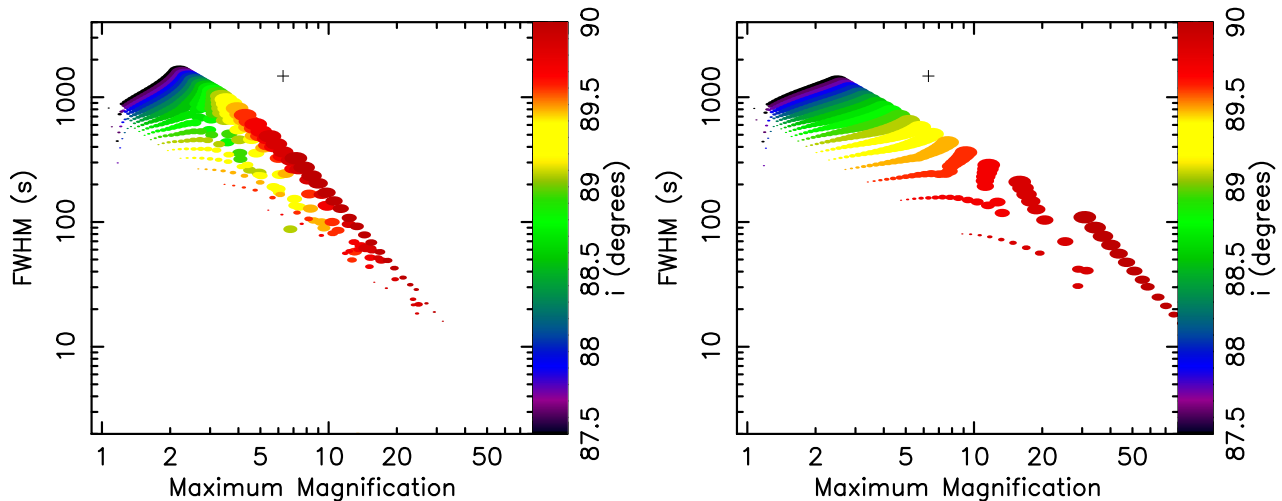


Figure 13. Lensing flare FWHM versus peak magnification for an aligned ($\delta = \gamma = 0^\circ$) binary system with spin parameter $a = 0$ (left) and $a = 0.998$ (right). Binary mass is varied in the range $M = 5 \times 10^4 - 5 \times 10^6 M_\odot$, with larger markers corresponding to larger mass. Inclination angle is denoted by the colour code. The black cross corresponds to the QPEs in GSN 069.

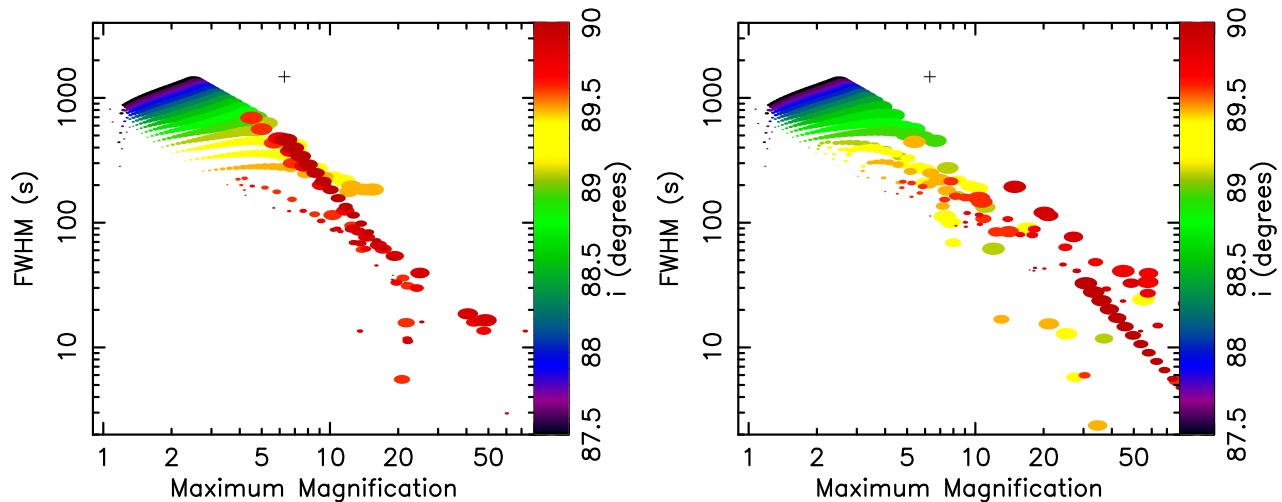


Figure 14. Lensing flare FWHM versus peak magnification for two configurations in which we view the underside of the source and lens disc ($\gamma = 180^\circ$). The BH spin parameter is $a = 0.998$. Left: $\delta = 0.5^\circ$; Right: $\delta = 1^\circ$. Binary mass is varied in the range $M = 5 \times 10^4 - 5 \times 10^6 M_\odot$, with larger markers corresponding to larger mass. Inclination angle is denoted by the colour code. The black cross corresponds to the QPEs in GSN 069.

QPEs observed for RX J1301 is consistent with the binary BH hypothesis as long as the current binary eccentricity is $\epsilon \gtrsim 0.16$. Since GW emission erodes eccentricity, lower eccentricity solutions are more likely, favouring lower binary masses; $M \lesssim 10^6 M_\odot$. The simulations of Zrake et al. (2021, see their fig. 4) imply that an even lower mass of $M \lesssim 10^4 M_\odot$ is required for a 9 h period, $q \sim 1$ binary to have an eccentricity of $\epsilon \gtrsim 0.1$. We cannot place eccentricity limits on GSN 069, but the \sim equal spacing between QPEs favours $\epsilon \sim 0$. In addition to orbital decay via GW emission reducing the orbital period over time, periastron precession will evolve the relative waiting times between the large and small flares in the two-flare QPE cycle, if $\epsilon > 0$. The model therefore predicts such an effect to occur for RX J1301 (periastron precession period of ~ 1 yr) but not for GSN 069. However, we have not been able to reproduce the flare profiles with the self-lensing model. Self-lensing flares are either the correct amplitude but too sharp, or the correct duration but too

weak. Moreover, the model can reproduce stronger flares in harder energy bands due to the brighter parts of the background accretion disc radiating a harder spectrum, but the energy dependence of the predicted self-lensing flares is far more subtle than that observed for QPEs.

The discrepancy between the predicted and observed flare profiles is relatively small – there are solutions with the correct amplitude but FWHM $\sim 2/5$ of the observed value, and those with the correct FWHM and amplitudes $\sim 2/5$ of the observed value. It is therefore possible that improving on some of the simplified assumptions in the model may in future enable it to reproduce the observed flare profiles. For example, we account for lensing by the foreground BH using the formula relevant to e.g. lensing of background galaxies by a foreground cluster (e.g. Walsh, Carswell & Weymann 1979) or micro-lensing via chance alignments in our galaxy (e.g. Paczyński 1986; Agol 2002), which ignores strong field effects (Schnittman

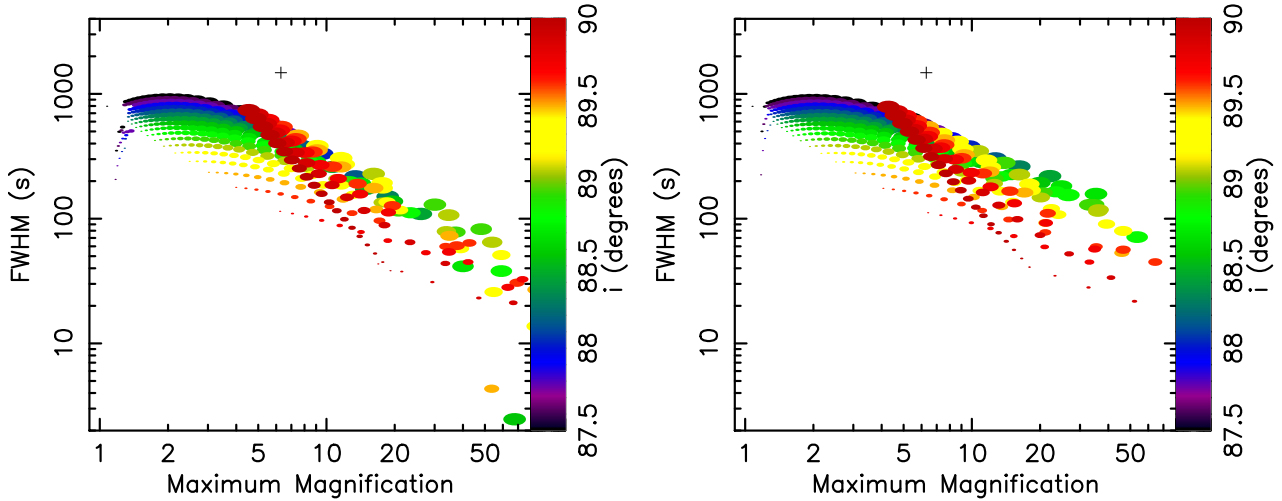


Figure 15. Lensing flare FWHM versus peak magnification for two configurations in which we view the source and lens discs edge-on ($\gamma = 90^\circ$). The BH spin parameter is $a = 0.998$. Left: $\delta = 70^\circ$, Right: $\delta = 90^\circ$. Binary mass is varied in the range $M = 5 \times 10^4 - 5 \times 10^6 M_\odot$, with larger markers corresponding to larger mass. Inclination angle is denoted by the colour code. The black cross corresponds to the QPEs in GSN 069.

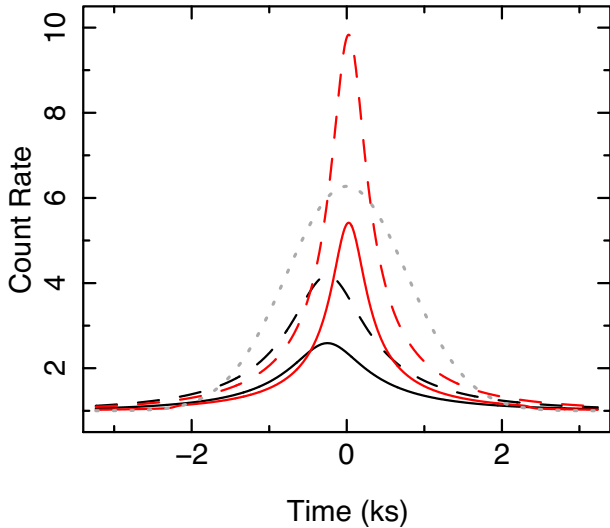


Figure 16. 0.4–2 keV light curves for the model parameters closest to reproducing the properties of the GSN 069 QPE flares. The black lines are the best aligned ($\delta = 0$) model and the red lines are the best overall model ($\delta = \gamma = 90^\circ$). See text for the other parameters. The dashed lines are without occultation by the foreground mini-disc, and the solid lines are with occultation. The grey dotted line represents the average GSN 069 flare profile.

et al. 2018). In particular, rays passing close to a spinning BH are preferentially concentrated to one side of the Einstein ring instead of being uniformly concentrated around it (e.g. Yang & Wang 2013), which will likely increase the magnification and also the energy dependence of the flares, as different regions of the background mini-disc will be magnified more as the foreground BH passes in front of them. We also employ an approximate prescription for Shapiro delays. While we do limit our parameter exploration to equal mass ratio binaries, we note that any relaxation of this assumption that has a large effect on the flare amplitude will also predict a bigger ratio between the amplitude of large and small flares than is observed. There are, however, many simplifying assumptions we have made

about the properties of the mini-discs that could be relaxed in future. Allowing them to be optically thin would automatically increase the flare amplitudes by reducing occultation of the background disc by the foreground disc. However, this would need to be justified by demonstrating that the spectrum of the QPE sources is consistent with being non-thermal. The discs may also have a non-zero scale height, may not be perfectly aligned with their BH spin axis, may be mildly truncated outside of the ISCO, may have a shallower emissivity profile than the canonical r^{-3} relation, their outer radii may be different from what we assume here, or the gas streams between mini-discs and from circumbinary disc to mini-discs that we ignore here may in reality be important. We also do not include a compact corona close to each BH in our model. This is driven by the X-ray spectrum of GSN 069 and RX J1301 being disc-dominated, although there is evidence for a weak power-law component in the spectrum of RX J1301 (Middleton & Ingram 2015). It is therefore still possible for the self-lensing model to yet reproduce the observed QPE profiles, but it is harder to imagine the model being able to reproduce the flare profiles for a reasonably large part of parameter space so as not to be fine-tuned, or reproducing the strong energy dependence of the observed flares. We therefore conclude that the two QPE sources could in principle be binary BH systems, but that the mechanism for the flares is unlikely to be lensing of the background mini-disc by the foreground BH.

It is also important to note that very close binaries, within ~ 100 yr of merger, must be rare in the local Universe, since this phase is a small fraction of the overall binary lifetime. This favours lower binary mass in our model, since lower mass binaries with a given period are further from merger (see e.g. Fig. 3). This requirement is in tension with the flare profile modelling, which is closer to reproducing the observed flares for high lens mass. In any case, this consideration means that the model requires QPEs with short flare spacings to be rare. Similar sources with much larger spacings between flares may be much more common, but such flares are potentially easier to miss.

The discovery of close binary massive BH systems in the GW inspiral phase is a very important goal in astrophysics that as yet remains elusive. Such systems are thought to be important diagnostics of galaxy evolution, since galaxy mergers result in the central BHs of the two constituent galaxies forming an initially wide

binary that eventually decays down to ~ 1 pc separation via dynamical friction (e.g. Barnes & Hernquist 1996; Barnes 2002; Mayer 2013). It is unclear how binary systems then become close enough for GW emission to efficiently evolve the orbit (*the final parsec problem*: Begelman, Blandford & Rees 1980; Milosavljević & Merritt 2003; Armitage & Natarajan 2005), eventually resulting in a merger with a detectable GW signal. Discovery of a close binary system via electromagnetic emission will therefore definitively confirm that at least nature knows how to solve the final parsec problem, and will provide important constraints on the expected merger rates for *LISA*.

Wide (separation $\gg 1$ pc) accreting BH–BH binary systems can be identified using high-resolution observations (X-ray: Komossa et al. 2003; Comerford et al. 2015; optical: Comerford et al. 2015; Goulding et al. 2019; Kollatschny et al. 2020; radio: Rodriguez et al. 2006; Fu et al. 2015; Kharb, Lal & Merritt 2017), but other indirect methods are required to identify close binaries in the GW inspiral phase (separation $\lesssim 0.01$ pc). Proposed diagnostics include a broad dip in the disc blackbody spectrum caused by the cavity opened up by tidal forces (Roedig, Krolik & Miller 2014 – although this dip was not recovered in the simulations of Farris et al. 2015 and d’Ascoli et al. 2018 since emission from the accretion streams compensates for the presence of the cavity), a ‘ripple shaped’ iron $K\alpha$ line caused by Doppler shifts from the two orbiting mini-discs (McKernan et al. 2013), a periodicity due to Doppler boosting of the orbiting mini-discs (D’Orazio, Haiman & Schiminovich 2015) and quasi-periodic oscillations due to interactions between the mini-discs and the circumbinary disc (MacFadyen & Milosavljević 2008; D’Orazio et al. 2013; Farris et al. 2014, 2015; Shi & Krolik 2015). More than 100 candidate sub-pc binaries have been identified by searching for periodicities in large optical surveys (e.g. Lehto & Valtonen 1996; Graham et al. 2015a, b; Charisi et al. 2016; see fig. 2 in D’Orazio & Di Stefano 2018 for a compilation). However, none have been definitively confirmed as binary systems, largely because AGNs ubiquitously display strong red noise variability that is very likely to appear quasi-periodic for several cycles, particular when large data sets are considered without adequately accounting for the large number of trials (Vaughan et al. 2016). Also, true quasi-periodic behaviour is not exclusive to binary BH–BH systems (e.g. Ingram & Motta 2019). Indeed, a sample of seven objects identified as binary candidates via periodicity claims was recently found to have X-ray spectral properties indistinguishable from the general AGN population (Saade et al. 2020). Self-lensing flares have been suggested as a distinctive signature of high inclination accreting binary BH systems (Haiman 2017; D’Orazio & Di Stefano 2018), and one candidate system, nicknamed *Spikey*, has been identified in archival *Kepler* data (Hu et al. 2020; Kun et al. 2020). The light curve of *Spikey* can be modelled with a self-lensing flare plus Doppler modulation from a binary system with parameters $\epsilon \approx 0.5$, $P \approx 418$ d, $M \approx 3 \times 10^7 M_{\odot}$, $i \approx 82^{\circ}$, and the model predicts another lensing flare to happen this year.

The modelling we have presented here builds upon earlier work (Haiman 2017; D’Orazio & Di Stefano 2018) by including more relativistic effects and, most crucially, including occultation by the foreground mini-disc. This gives rise to a variety of behaviours: different parameters lead to flares (e.g. Fig. 7), eclipses (e.g. Fig. 9), and eclipses with a central narrow flare (e.g. Fig. 11). In particular, the eclipse with a central flare is an extremely distinctive feature that can be searched for in X-ray survey data (e.g. *XMM–Newton*, *eROSITA*). In future, we will extend our modelling to determine if any similarly distinctive features are predicted in the optical, which can then be searched for in surveys such as *ZTF* and *LSST*. For example, two very sharp flares may occur during the eclipse as the outer part of the

background mini-disc twice passes close to the Einstein radius of the foreground BH (i.e. first, right-hand side of the disc as we see it, then the left-hand side), or lensing of emission from the circumbinary disc by the two BHs could cause a flare if the binary plane is misaligned with the circumbinary disc. If such a feature were to be discovered, it would constitute very strong evidence for the presence of a binary SMBH system. We note that such a discovery would require the molecular torus associated with the AGN to either be misaligned with the binary plane (which is plausible, for instance the AGN accretion disc orientation does not appear to be correlated with that of the host galaxy’s stellar disc: Middleton et al. 2016), or to have not yet fully formed (under a paradigm whereby most AGN activity is triggered by galaxy mergers).

If the QPEs from GSN 069 and RX J1301 are not due to self-lensing, then what are they caused by? It could be that the system is a binary, but with a very low mass ratio $q \lesssim 10^{-2}$ such that the flares are instead caused by the secondary crashing through the primary’s accretion disc twice per orbital period – as is suggested for the much more massive ($M \sim 1.71 \times 10^{10} M_{\odot}$, $q \sim 6 \times 10^{-3}$) AGN OJ287 (Lehto & Valtonen 1996). We note that in this scenario, the requirement for QPEs to be very rare is relaxed a lot compared with the lensing model since such a system would be far from merging and does not need to be viewed from a special angle, plus minor mergers are more frequent than major mergers. Alternatively, King (2020) suggested that the QPEs in GSN 069 result from a ‘near-miss’ tidal disruption event (TDE) of a red giant whose envelope was stripped, leaving behind a white dwarf core (current mass $\sim 0.21 M_{\odot}$) on an eccentric orbit (current eccentricity $\epsilon_0 \sim 0.94$) around a single $M \sim 4 \times 10^5 M_{\odot}$ BH. In this case, the QPE flares occur due to enhanced accretion each time the orbit reaches pericentre. This model nicely explains the factor $\gtrsim 240$ rise in the quiescent flux level of GSN 069 between a *ROSAT* non-detection in 1994 and the first *XMM–Newton* detection in 2010 (i.e. the near-miss TDEs assumed to have occurred at some time during the intervening 16 yr), followed by the subsequent onset of QPEs and slow decay of the quiescent flux level. In our self-lensing picture, there is no ready interpretation for the rise in the quiescent flux level, but the sudden onset of QPEs could in principle be explained by the orbital separation becoming small enough for lensing flares to begin (the lensing amplitude can be a steep function of impact parameter for certain values of impact parameter). The failed TDE model, however, struggles to explain the symmetric nature of the QPEs (accretion flares have a fast rise, exponential decay profile). It also cannot reproduce the long-waiting-time-followed-by-short-waiting-time behaviour of the QPEs, particularly for RX J1301 in which this behaviour is much more pronounced.

It has alternatively been suggested (Miniutti et al. 2019) that QPEs could be due to limit-cycle accretion rate variations, analogous to the ‘heartbeat’ oscillations observed from Galactic X-ray binaries GRS 1915+105 (Belloni et al. 2000), IGR J17091–3624 (Altamirano et al. 2011) and the Rapid Burster (Bagnoli & in’t Zand 2015), and the ultra-luminous X-ray source NGC 3621 (Motta et al. 2020). However, the duration of QPEs are far fewer dynamical time-scales than the duration of any heartbeat flares in lower mass systems, and it is difficult to imagine how accretion variation could lead to such sharp, symmetric flares on a time-scale \sim one hundredth of a viscous time-scale. Miniutti et al. (2019) argue that ‘changing-look’ AGNs also vary faster than the viscous time-scale and therefore standard accretion theory may simply be missing something, but we do not know that changing-look AGNs are driven by intrinsic accretion changes. Another model, suggested for RX J1301 before the GSN 069 QPEs were discovered, is the ‘Swiss cheese’ model

of Middleton & Ingram (2015). This assumes that a low-mass AGN is surrounded by an optically thick shroud of orbiting material. A hole in the shroud then reveals the centre of the disc each time it orbits into the line of sight. This model can qualitatively describe the spectral evolution of the only QPE that was known at the time (the single full flare in the 2000 *XMM-Newton* observation of RX J1301). However, it does not explain the long-waiting-time-followed-by-short-waiting-time behaviour, and it also seems unlikely that a hole in a similar part of the shroud would still be there 19 yr after the first QPE was observed. Most recently, Raj & Nixon (2021) suggested that QPE flares could be produced by disc tearing, which has been shown in simulations to occur due to the frame dragging effect when the disc is highly inclined to the BH spin axis. This model can reproduce the observed flare amplitude, but the predicted flares are more asymmetric than the observed flares, and it does not naturally explain the long-waiting-time-followed-by-short-waiting-time behaviour.

5 CONCLUSIONS

We have explored a self-lensing binary SMBH model for the sharp flares (QPEs) exhibited by the low-mass AGNs GSN 069 and RX J1301. Our model can reproduce the observed QPE recurrence times if the current eccentricity of RX J1301 is $\epsilon_0 \gtrsim 0.16$, and the evolution of recurrence times in observations of RX J1301 separated by ~ 19 yr suggests a total binary mass $\lesssim 10^6 M_\odot$ that will merge within the next ~ 1000 yr. However, we have been unable to reproduce the observed flare profiles with our gravitational self-lensing model – predicting either flares of the correct amplitude that are too sharp, or flares of the correct duration that are too low in amplitude. We conclude that self-lensing is unlikely to be the mechanism behind the observed QPEs, although we note that improving upon some of the simplified assumptions employed in this paper may yet enable to model to reproduce the observed flares. Several models have been suggested for QPEs, but none can currently reproduce the full array of observational properties.

Self-lensing remains a promising means for discovering binary SMBH systems in future. Our modelling extends upon previous work by including more GR effects and, most significantly, occultation of the background mini-disc by the foreground mini-disc. We find three distinctive behaviours: (i) lensing flares with occultation slightly reducing the peak magnification, (ii) partial eclipses (in-eclipse flux originates from the foreground mini-disc) with no associated lensing flare, and (iii) partial eclipses with a very sharp in-eclipse lensing flare. All three behaviours are distinctive diagnostics of binary SMBH systems that can be searched for in current and future surveys (e.g. *eROSITA*, *ZTF*, *LSST*) to identify binaries and to place strong constraints on their properties.

ACKNOWLEDGEMENTS

We thank the anonymous referee for insightful comments that improved the paper. We acknowledge valuable discussions with Giovanni Miniutti and Margherita Giustini. A.I. acknowledges support from the Royal Society and fruitful discussions with Andrew King, Matt Middleton, Philipp Podsiadlowski, Andy Mummery, and Rob Fender. S.A. acknowledges support from the STFC (grant numbers ST/N000919/1 and ST/R004846/1). The scientific results reported in this work are based on observations obtained with *XMM-Newton*, an ESA science mission with instruments and contributions directly funded by ESA Member States and NASA, and the Chandra X-ray Observatory.

DATA AVAILABILITY

The data underlying this article, including all source code, will be shared on reasonable request to the corresponding author.

REFERENCES

- Abarr Q., Krawczynski H., 2020, *ApJ*, 889, 111
 Agol E., 2002, *ApJ*, 579, 430
 Altamirano D. et al., 2011, *ApJ*, 742, L17
 Amaro-Seoane P. et al., 2017, preprint (arXiv:1702.00786)
 Armitage P. J., Natarajan P., 2005, *ApJ*, 634, 921
 Artymowicz P., Lubow S. H., 1994, *ApJ*, 421, 651
 Bagnoli T., in 't Zand J. J. M., 2015, *MNRAS*, 450, L52
 Bardeen J. M., Petterson J. A., 1975, *ApJ*, 195, L65
 Bardeen J. M., Press W. H., Teukolsky S. A., 1972, *ApJ*, 178, 347
 Barnes J. E., 2002, *MNRAS*, 333, 481
 Barnes J. E., Hernquist L., 1996, *ApJ*, 471, 115
 Begelman M. C., Blandford R. D., Rees M. J., 1980, *Nature*, 287, 307
 Belloni T., Klein-Wolt M., Méndez M., van der Klis M., van Paradijs J., 2000, *A&A*, 355, 271
 Bowen D. B., Campanelli M., Krolik J. H., Mewes V., Noble S. C., 2017, *ApJ*, 838, 42
 Bowen D. B., Mewes V., Campanelli M., Noble S. C., Krolik J. H., Zilhão M., 2018, *ApJ*, 853, L17
 Charisi M., Bartos I., Haiman Z., Price-Whelan A. M., Graham M. J., Bellm E. C., Laher R. R., Márka S., 2016, *MNRAS*, 463, 2145
 Comerford J. M., Pooley D., Barrows R. S., Greene J. E., Zakamska N. L., Madejski G. M., Cooper M. C., 2015, *ApJ*, 806, 219
 d'Ascoli S., Noble S. C., Bowen D. B., Campanelli M., Krolik J. H., Mewes V., 2018, *ApJ*, 865, 140
 D'Orazio D. J., Di Stefano R., 2018, *MNRAS*, 474, 2975
 D'Orazio D. J., Haiman Z., MacFadyen A., 2013, *MNRAS*, 436, 2997
 D'Orazio D. J., Haiman Z., Schiminovich D., 2015, *Nature*, 525, 351
 Dewangan G. C., Singh K. P., Mayya Y. D., Anupama G. C., 2000, *MNRAS*, 318, 309
 Dexter J., Agol E., 2009, *ApJ*, 696, 1616
 Done C., Gierlinski M., Kubota A., 2007, *A&A*, 15, 1
 Duffell P. C., D'Orazio D., Derdzinski A., Haiman Z., MacFadyen A., Rosen A. L., Zrake J., 2020, *ApJ*, 901, 25
 Farris B. D., Duffell P., MacFadyen A. I., Haiman Z., 2014, *ApJ*, 783, 134
 Farris B. D., Duffell P., MacFadyen A. I., Haiman Z., 2015, *MNRAS*, 446, L36
 Frank J., King A., Raine D. J., 2002, *Accretion Power in Astrophysics*, 3rd edn. Cambridge Univ. Press, Cambridge
 Fu H., Wrobel J. M., Myers A. D., Djorgovski S. G., Yan L., 2015, *ApJ*, 815, L6
 Giustini M., Miniutti G., Saxton R. D., 2020, *A&A*, 636, L2
 Gopakumar A., Iyer B. R., 1997, *Phys. Rev. D*, 56, 7708
 Goulding A. D., Pardo K., Greene J. E., Mingarelli C. M. F., Nyland K., Strauss M. A., 2019, *ApJ*, 879, L21
 Graham M. J. et al., 2015a, *MNRAS*, 453, 1562
 Graham M. J. et al., 2015b, *Nature*, 518, 74
 Haiman Z., 2017, *Phys. Rev. D*, 96, 023004
 Hu B. X., D'Orazio D. J., Haiman Z., Smith K. L., Snios B., Charisi M., Di Stefano R., 2020, *MNRAS*, 495, 4061
 Ingram A. R., Motta S. E., 2019, *New Astron. Rev.*, 85, 101524
 Ingram A., van der Klis M., Middleton M., Altamirano D., Uttley P., 2017, *MNRAS*, 464, 2979
 Ingram A., Mastroserio G., Dauser T., Hovenkamp P., van der Klis M., García J. A., 2019, *MNRAS*, 488, 324
 Key J. S., Cornish N. J., 2011, *Phys. Rev. D*, 83, 083001
 Kharb P., Lal D. V., Merritt D., 2017, *Nat. Astron.*, 1, 727
 King A., 2020, *MNRAS*, 493, L120
 Kollatschny W., Weibacher P. M., Ochmann M. W., Chelouche D., Monreal-Ibero A., Bacon R., Contini T., 2020, *A&A*, 633, A79

- Komossa S., Burwitz V., Hasinger G., Predehl P., Kaastra J. S., Icke Y., 2003, *ApJ*, 582, L15
- Kun E., Frey S., Gabányi K. É., 2020, *MNRAS*, 496, 3336
- Lehto H. J., Valtonen M. J., 1996, *ApJ*, 460, 207
- Liska M., Hesp C., Tchekhovskoy A., Ingram A., van der Klis M., 2019, *MNRAS*, 487, 550L
- Lynden-Bell D., Pringle J. E., 1974, *MNRAS*, 168, 603
- MacFadyen A. I., Milosavljević M., 2008, *ApJ*, 672, 83
- Martel K., Poisson E., 1999, *Phys. Rev. D*, 60, 124008
- Mayer L., 2013, *Class. Quantum Gravity*, 30, 244008
- McKernan B., Ford K. E. S., Kocsis B., Haiman Z., 2013, *MNRAS*, 432, 1468
- Middleton M. J., Ingram A. R., 2015, *MNRAS*, 446, 1312
- Middleton M. J., Parker M. L., Reynolds C. S., Fabian A. C., Lohfink A. M., 2016, *MNRAS*, 457, 1568
- Milosavljević M., Merritt D., 2003, *ApJ*, 596, 860
- Miniutti G. et al., 2019, *Nature*, 573, 381
- Misner C. W., Thorne K. S., Wheeler J. A., 1973, *Gravitation*. W.H. Freeman and Co., San Francisco
- Motta S. E. et al., 2020, *ApJ*, 898, 174
- Mushtukov A. A., Ingram A., van der Klis M., 2018, *MNRAS*, 474, 2259
- Novikov I. D., Thorne K. S., 1973, in Dewitt C., Dewitt B. S., eds, *Black Holes (Les Astres Occlus)*. Gordon and Breach, New York, p. 343
- Paczynski B., 1986, *ApJ*, 304, 1
- Paczynski B., 1996, *ARA&A*, 34, 419
- Paschalidis V., Bright J., Ruiz M., Gold R., 2021, preprint ([arXiv:2102.06712](https://arxiv.org/abs/2102.06712))
- Peters P. C., 1964, *Phys. Rev.*, 136, 1224
- Pringle J. E., 1991, *MNRAS*, 248, 754
- Raj A., Nixon C. J., 2021, *ApJ*, 909, 82
- Robson T., Cornish N. J., Liu C., 2019, *Class. Quantum Gravity*, 36, 105011
- Rodriguez C., Taylor G. B., Zavala R. T., Peck A. B., Pollack L. K., Romani R. W., 2006, *ApJ*, 646, 49
- Roedig C., Krolik J. H., Miller M. C., 2014, *ApJ*, 785, 115
- Ryan G., MacFadyen A., 2017, *ApJ*, 835, 199
- Saade M. L. et al., 2020, *ApJ*, 900, 148
- Schnittman J., Baker J., Etienne Z., Giacomazzo B., Kelly B., 2018, in *American Astronomical Society Meeting Abstracts*, Vol. 231. p. 405
- Shakura N. I., Sunyaev R. A., 1973, *A&A*, 24, 337
- Shi J.-M., Krolik J. H., 2015, *ApJ*, 807, 131
- Shu X. W., Wang S. S., Dou L. M., Jiang N., Wang J. X., Wang T. G., 2018, *ApJ*, 857, L16
- Sun L., Shu X., Wang T., 2013, *ApJ*, 768, 167
- Tang Y., Haiman Z., MacFadyen A., 2018, *MNRAS*, 476, 2249
- Vaughan S., Uttley P., Markowitz A. G., Huppenkothen D., Middleton M. J., Alston W. N., Scargle J. D., Farr W. M., 2016, *MNRAS*, 461, 3145
- Walsh D., Carswell R. F., Weymann R. J., 1979, *Nature*, 279, 381
- Wang Z.-Y., Huang C.-Y., Wang D.-X., Wang J.-Z., 2012, *Res. Astron. Astrophys.*, 12, 661
- Wilms J., Allen A., McCray R., 2000, *ApJ*, 542, 914
- Yang X., Wang J., 2013, *ApJS*, 207, 6
- Zrake J., Tiede C., MacFadyen A., Haiman Z., 2021, *ApJ*, 909, L13

APPENDIX A: DETAILS OF LENSING FLARES MODEL

A1 Coordinate system

The observer's line of sight is

$$\hat{\mathbf{o}} = \sin i \cos \phi_i \hat{\mathbf{x}}_{\text{bin}} + \sin i \sin \phi_i \hat{\mathbf{y}}_{\text{bin}} + \cos i \hat{\mathbf{z}}_{\text{bin}}, \quad (\text{A1})$$

such that projected distance on the observer's sky between the two BHs is smallest when the orbital phase is $\phi_* = \phi_i$. The rotation axis

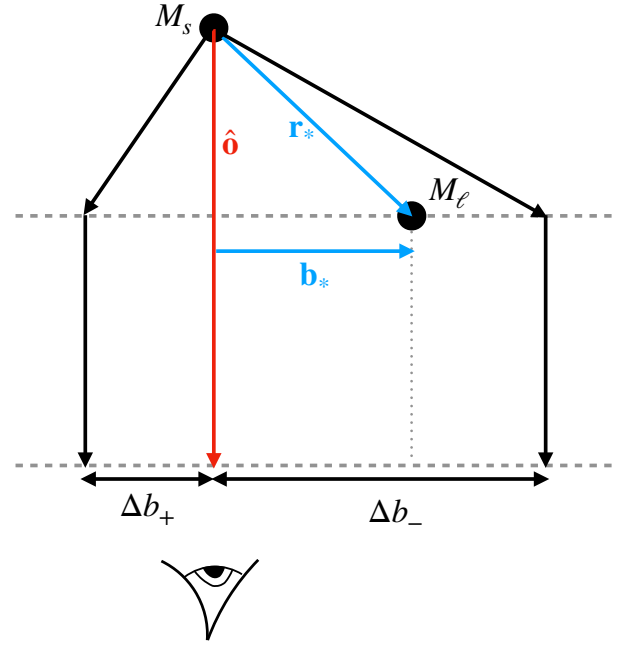


Figure A1. Schematic illustrating the path-length of photons for the internal image (black arrows on the right) and the external image (black arrows on the left). See text for further details.

of the background (source) mini-disc is

$$\hat{\mathbf{z}}_s = \sin \delta_s \cos(\phi_i - \gamma_s) \hat{\mathbf{x}}_{\text{bin}} + \sin \delta_s \sin(\phi_i - \gamma_s) \hat{\mathbf{y}}_{\text{bin}} + \cos \delta_s \hat{\mathbf{z}}_{\text{bin}}. \quad (\text{A2})$$

The expression for $\hat{\mathbf{z}}_\ell$ is the same with s subscripts replaced by ℓ subscripts.

The image plane is perpendicular to $\hat{\mathbf{o}}$. It is convenient to define the vertical axis of the image plane as the projection of the BH spin axis on the image plane. Since the two BHs can have different spin axes to one another, we define one vertical axis for the background BH, $\hat{\beta}_s$, and another for the foreground BH, $\hat{\beta}_\ell$. The horizontal axis of the image plane for the background BH is therefore

$$\hat{\alpha}_s = \frac{\hat{\mathbf{z}}_s \times \hat{\mathbf{o}}}{|\hat{\mathbf{z}}_s \times \hat{\mathbf{o}}|}, \quad (\text{A3})$$

and the vertical axis is $\hat{\beta}_s = \hat{\mathbf{o}} \times \hat{\alpha}_s$, with similar expressions for $\hat{\alpha}_\ell$ and $\hat{\beta}_\ell$. In the main text, we simply use α , β , and \mathbf{b} and specify which definition of the image plane we are referring to.

The vector $\mathbf{b}_* = \alpha_* \hat{\alpha}_s + \beta_* \hat{\beta}_s$, where $\alpha_* = \mathbf{r}_* \cdot \hat{\alpha}_s$ and $\beta_* = \mathbf{r}_* \cdot \hat{\beta}_s$, points on the image plane from the centre of the source BH to the centre of the lens BH. The vectors \mathbf{b}_s and \mathbf{b}_ℓ are also defined on the image plane. \mathbf{b}_s points from the source BH to a given point on the source disc, and \mathbf{b}_ℓ points from the lens BH to a given point on the lens disc. The vector that points from the lens BH to a given point on the source disc is therefore $\mathbf{b}_s - \mathbf{b}_*$. We can determine if a given point on the background (source) is eclipsed by the foreground (lens) disc by comparing the vectors \mathbf{b}_ℓ and $\mathbf{b}_s - \mathbf{b}_*$.

A2 Shapiro delays

Fig. A1 illustrates the approximate path of rays from a source very close to the background BH (labelled M_s), around the foreground BH (labelled M_ℓ), and finally towards the observer (bottom). The vector \mathbf{r}_* points from the background BH to the foreground BH, \mathbf{b}_* is the

projection of \mathbf{r}_* on the image plane, and $\hat{\mathbf{o}}$ points from the source BH towards the observer. In the absence of the foreground BH, the image would be at the origin in this example. Instead, there are two images: the internal image at Δb_- , and the external image at Δb_+ . The rays for each image, denoted by the black arrows, have a longer path-length than an un-lensed ray, which would travel along $\hat{\mathbf{o}}$ (red arrow). This extra path-length is

$$c \Delta t_{\pm}(\phi_*) = \sqrt{(\mathbf{r}_*(\phi_*) \cdot \hat{\mathbf{o}})^2 + (\Delta b_{\pm})^2} - \mathbf{r}_*(\phi_*) \cdot \hat{\mathbf{o}}, \quad (\text{A4})$$

where Δt_{\pm} is the Shapiro delay. This is an approximate treatment of the Shapiro delay since in reality the geodesics are not straight lines with a sharp bend, and there are also Shapiro delays due to lensing around the background BH. Also, the above formula assumes that the source is very small compared with the binary separation. In other words, it assumes that $r \ll r_*$ for all disc patches. This is not the case for the outer disc ($r_{\text{out}} = 0.25 r_*$), but the X-ray flux is dominated by light from the inner disc due to the steep gravitational emissivity. A more accurate treatment of Shapiro delays would therefore be required for the optical signal, for which the emissivity is less centrally peaked.

We calculate $\Delta t_{\pm}(\phi_*)$ for the orbital phase corresponding to the time the photon was emitted, $\phi_*(t_{\text{em}})$. The photon crosses the top grey dashed line in Fig. A1 (after which all geodesics have the same light traveltime) at time $t = t_{\text{em}} + \Delta t_{\pm}[\phi_*(t_{\text{em}})]$. Practically, we start by specifying the time t (which is the same for every pixel of the

image), and use an iteration scheme to calculate t_{em}

$$t_{\text{em}(i+1)} = t - \Delta t_{\pm}[\phi_*(t_{\text{em}(i)})], \quad (\text{A5})$$

where we set $t_{\text{em}(0)} = t$. The iteration scheme converges very quickly, typically after a few steps.

A3 Disc spectrum

For each time bin and for each patch of the background mini-disc, we calculate the position of the two images of the patch on the image plane, and assess if either of these are eclipsed by the foreground disc. The specific flux of the background mini-disc at time t is

$$F_s(E, t) \propto \int_{\alpha_s, \beta_s} [\eta_+(t)\mathcal{M}_+(t) + \eta_-(t)\mathcal{M}_-(t)] \times g^3 I(E/g, T) d\alpha_s d\beta_s, \quad (\text{A6})$$

where η_{\pm} is 0 if the image of the background disc patch is eclipsed by the foreground disc and 1 otherwise. \mathcal{M}_{\pm} is the magnification, given by equation (7) in the main text. $I(E, T)$ is the specific intensity radiated by the disc at coordinates r, ϕ , which we assume to be a blackbody with the temperature profile given in the main text. g is the blueshift experienced by a photon travelling from the disc patch to the observer (see equation 4 of Ingram et al. 2017).

This paper has been typeset from a $\text{\TeX}/\text{\LaTeX}$ file prepared by the author.